

# A comparison between four different retrieval methods for ice-cloud properties using data from the CloudSat, CALIPSO, and MODIS satellites

THORWALD H. M. STEIN \* JULIEN DELANOË, AND ROBIN J. HOGAN

*Department of Meteorology, University of Reading, United Kingdom*

## ABSTRACT

The A-Train constellation of satellites provides a new capability to measure vertical cloud profiles leading to more detailed information on ice-cloud microphysical properties than has been possible up to now. A variational radar-lidar ice-cloud retrieval algorithm, VarCloud, takes advantage of the complementary nature of the CloudSat radar and CALIPSO lidar to provide a seamless retrieval of ice water content, effective radius and extinction coefficient from the thinnest cirrus (seen only by the lidar) to the thickest ice cloud (penetrated only by the radar). In this paper, several versions of the VarCloud retrieval are compared with the CloudSat standard ice-only retrieval of ice water content, two empirical formulas that derive ice water content from radar reflectivity and temperature, and retrievals of vertically integrated properties from the MODIS radiometer. Typically the retrieved variables agree within a factor of 2, on average, and most of the differences can be explained by the different microphysical assumptions. For example, the ice water content comparison illustrates the sensitivity of the retrievals to assumed ice particle shape. If ice particles are modeled as oblate spheroids rather than spheres for radar scattering then the retrieved ice water content is reduced by on average 35% in clouds with a reflectivity factor larger than 0 dBZ. The factor-of-2 difference between MODIS and VarCloud optical depth, on average, can be explained by the different assumptions on particle mass and area; if VarCloud mimics the MODIS assumptions then better agreement is found in both optical depth and effective radius. However, MODIS predicts the mean vertically integrated ice water content to be around a factor-of-3 lower than VarCloud for the same retrievals, because the MODIS algorithm assumes that its retrieved effective radius (which is mostly representative of cloud top) is constant throughout the depth of the cloud. These comparisons highlight the need to refine microphysical assumptions in all retrieval algorithms, and also for future studies to compare not only the mean values but also the full probability density function.

## 1. Introduction

The advent of satellite observations has provided access to cloud data from across the globe and their statistics allow for the creation of cloud climatologies (Warren and Hahn 2002). These global cloud observations are vital to set constraints on general circulation models (GCMs), which show factors of 10 or more difference in ice water path (IWP), but the current satellite cloud-ice retrievals often disagree due to varying footprints and instrument and algorithm sensitivities (Waliser et al. 2009). The A-Train constellation of satellites take various measurements of ice clouds (Stephens et al. 2002), starting with the launch of Aqua in 2002, carrying the Moderate Resolution Imaging Spectroradiometer (MODIS), which retrieves cloud optical properties using shortwave and infrared radiances. In 2006, Aqua was joined by the CloudSat radar and the Cloud-Aerosol Lidar and Infrared Pathfinder Satellite Observation (CALIPSO) (Winker et al. 2003), providing vertical profiles of clouds around the globe on a daily basis. These

near-coincident measurements are ideal for combined retrieval techniques and to compare single-instrument cloud-ice retrievals.

The synergy of coincident radar and lidar observations is well documented (Intrieri et al. 1993; Donovan et al. 2001; Okamoto et al. 2003; Mitrescu et al. 2005; Tinel et al. 2005; Hogan et al. 2006a) and is already used to accurately determine the occurrence of hydrometeor layers by CloudSat and CALIPSO (Mace et al. 2009). Delanoë and Hogan (2008) developed an optimal estimation algorithm to retrieve cloud-ice properties from ground-based radar and lidar observations and recently adapted it to CloudSat and CALIPSO (Delanoë and Hogan 2010). A combined radar-lidar algorithm can retrieve ice particle size and concentration independently, and better estimates of these variables are obtained than if a single instrument were used (Hogan et al. 2006a).

In this paper the coincident A-Train measurements are used to study algorithm and instrument sensitivities for

ice-cloud retrievals. The following methods are compared:

- i. The combined radar-lidar optimal estimation retrieval developed by Delanoë and Hogan (2010), hereafter *VarCloud*;
- ii. The radar-only, ice-only version of the standard CloudSat product (Austin et al. 2009);
- iii. Two empirical formulas for ice water content (IWC) as a function of radar reflectivity factor  $Z$  and temperature  $T$ ,  $IWC(Z,T)$  (Hogan et al. 2006b; Protat et al. 2007);
- iv. The MODIS Level-2 Cloud Product (King et al. 1997).

The first three of these products retrieve IWC using at least two of the same inputs, namely the equivalent radar reflectivity factor  $Z_e$  observed by the CloudSat satellite and temperature  $T$  along the CloudSat track provided by the European Centre for Medium-Range Weather Forecasts (ECMWF). A direct comparison of IWC retrievals is possible where the radar is sensitive to ice cloud, so that the dependence of deviations in IWC on either temperature or reflectivity can be analysed.

Cloud-ice retrievals strongly depend on the representation of ice particles in terms of their shape, size, and distribution (McFarquhar and Heymsfield 1998; Heymsfield et al. 2008). With the introduction of the different products in Section 2, we will also provide an overview of the ice particle assumptions made in each retrieval.

The results are presented fourfold, starting with Section 3 in which the global distribution of ice clouds with temperature will be discussed. A cloud classification using CloudSat and CALIPSO data is used to compare ice-cloud occurrence as observed by the radar and lidar individually and jointly. The different IWC retrievals are compared in Section 4 through the joint probability distribution of IWC versus temperature. Where differences between retrievals occur, the impact of instrument and algorithm sensitivities is discussed, including the effect of different ice particle assumptions. In Section 5, this comparison focuses on individual IWC retrievals and the mean fractional difference of IWC between the various methods.

Finally, vertically integrated ice-cloud retrievals are presented in Section 6. Since MODIS is not designed to provide vertical profiles, we compare it with the *VarCloud* product using the in-cloud zonal averages of IWP. The MODIS IWP is inferred from the retrieval of optical depth  $\tau$  and mean effective radius  $\langle r_e \rangle$  (King et al. 2006), which are retrieved by *VarCloud* and provide an additional comparison with MODIS.

## 2. Method

Here, we introduce the four different retrieval methods that will be used for comparison in this paper. For a quick

overview of the satellite products, Figure 1 shows vertical profiles and the optical depth of a single cloud observed by the A-Train in the South Atlantic. The ice particle assumptions for the variables of interest in this paper are discussed below for each product and are summarised in Table 1.

### a. *VarCloud*

A variational retrieval algorithm using ground-based lidar and radar data was introduced by Delanoë and Hogan (2008). This method has recently been adapted to accommodate the measurements from the CloudSat radar and CALIPSO lidar (Delanoë and Hogan 2010) and in the present paper is referred to as *VarCloud*.

In this retrieval, the lidar and radar data are first merged on to the same grid. The CloudSat radar provides a vertical profile of  $Z_e$  at approximately 1.5km horizontal and 240m vertical resolution. The CALIPSO lidar provides attenuated backscatter coefficient  $\beta$  at 333m horizontal resolution and at a variable vertical resolution of 30 to 60m in the troposphere. CloudSat reflectivities are linearly interpolated from their 240m vertical resolution on to a regular 60m grid, whilst the lidar signal is averaged horizontally on to the CloudSat 1.5km horizontal grid before being averaged up to the regular 60m vertical grid. A similar interpolation is performed on the ECMWF temperature, pressure, and humidity variables, which are from the short-range forecasts under the CloudSat track, so that the necessary inputs for the *VarCloud* algorithm are available on a regular 1.5km grid with 60m vertical resolution.

On this merged grid, the *VarCloud* target classification is performed (Delanoë and Hogan 2010) using the CloudSat cloud mask in the “2B-GEOPROF” product (Mace 2004) and the “Lidar Level 2 Vertical Feature Mask” (Anselmo et al. 2006). This classification scheme identifies a target as cloud when the lidar mask has identified cloud or when the radar mask reports a value of 30 or greater, which indicates a high confidence in cloud detection. Once a cloud has been determined, it is set to be ice phase when  $T_w < 0^\circ\text{C}$ , with the occurrence of supercooled liquid identified by a strong lidar backscatter signal. This cloud classification is used in combination with the instrument flag (radar, lidar, or both) to determine ice-cloud occurrence in Section 3.

The *VarCloud* method uses an optimal estimation formulation, in which an initial estimate of the cloud variables in a single vertical profile (the state vector) are used in a forward model to predict the observed variables in that profile (the observation vector). The state vector contains an estimate of the visible extinction coefficient  $\alpha_v$  in the geometric optics approximation at each vertical level, a vertically constant lidar extinction-to-backscatter ratio  $S$ , and variables describing the profile of the “normalised” number concentration introduced by Delanoë et al. (2005). The forward model then calculates at each vertical level the radar

reflectivity factor  $Z_e$  using a lookup table derived from rigorous scattering calculations, and the lidar backscatter coefficient  $\beta$  using a multiple-scattering model (Hogan 2006). The difference between the forward modelled observations and the actual observed variables is then used to refine the state vector using the Gauss-Newton method (Rodgers 2002). This process is repeated until convergence following a  $\chi^2$  test. The retrieval can be further constrained if additional measurements are available for forward modelling, for instance infrared radiances or cloud visible optical depth retrieved during the day by shortwave radiances, although this capability is not used in the present paper.

The VarCloud algorithm contains a rigorous treatment of errors, in which errors are attributed to assumptions in the forward model, to the error covariances of the *a priori* (number concentration and  $S$ ) as well as the observations. The inclusion of the *a priori* allows for the retrieval to proceed when only a single instrument is available. In the absence of lidar observations, the retrieval tends to behave similarly to a relationship for IWC as a function of  $Z_e$  and  $T$ , whilst in the absence of radar observations the *a priori* ensures that the retrieval behaves similarly to a constrained lidar-only retrieval, making use of the molecular return below the cloud as an optical depth constraint, when available. This results in a seamless retrieval between optically thin ice clouds only seen by lidar and deep ice clouds seen by radar only, through cloud seen by both instruments.

To investigate the dependence of the retrievals on microphysical assumptions, three versions of the VarCloud retrieval method are used. The standard VarCloud product (Delanoë and Hogan 2010) will be referred to as VarCloud-OA (for “oblate aggregates”) and uses the T-matrix method to perform scattering calculations assuming that ice particles can be approximated by horizontally aligned oblate spheroids with an axial ratio of 0.6 (Hogan et al. 2010). The VarCloud-SA (for “spherical aggregates”) assumes spherical shapes for radar scattering calculations using Mie theory. Both VarCloud-OA and VarCloud-SA use the Brown and Francis (1995) mass-diameter relationship for the ice particle model and in their scattering calculations. This relationship was found to provide a very accurate estimate of radar reflectivity by Hogan et al. (2006b). The VarCloud-BR (for “bullet rosette”) version is only introduced as a potentially better match with the MODIS ice particle assumptions, for which bullet rosettes dominate the ice particle mixtures (King et al. 1997; Platnick et al. 2002; Baum et al. 2005a). In VarCloud-BR, Mie theory is applied to perform radar scattering calculations, whilst the ice particle model uses the Mitchell (1996) mass-area-size relationship for bullet rosettes.

#### b. Standard CloudSat radar-only product

The “Level 2B Radar-Only Cloud Water Content” product (2B-CWC-RO) is provided by the NASA CloudSat

project (Austin et al. 2009). This product makes use of optimal estimation theory, in which a lognormal size distribution  $N(D)$  of ice particles is assumed,

$$N(D) = \frac{N_T}{\sqrt{2\pi}\omega D} \exp\left[\frac{-\ln^2(D/D_g)}{2\omega^2}\right], \quad (1)$$

with the particle number concentration ( $N_T$ ), the width of the distribution ( $\omega$ ), and the geometric mean diameter ( $D_g$ ) being the retrieved state variables at each radar range-gate, all three with temperature-dependent *a priori* assumptions. The forward model then simulates values of the radar reflectivity factor  $Z_e$  for comparison with the observations using the three size distribution parameters. First, (1) is used to calculate Rayleigh reflectivity, after which Mie theory is applied in the form of a correction factor parameterized using the size distribution parameters  $\omega$  and  $D_g$  (Benedetti et al. 2003) to obtain  $Z_e$ .

The radar-only CloudSat product provides IWC from two versions of the algorithm. In the standard version, separate ice and liquid retrievals are scaled linearly with temperature between 0°C and −20°C by adjusting the respective particle number concentrations, resulting in a profile with ice-only retrievals at temperatures below −20°C and a smooth transition to liquid-only retrievals at temperatures above 0°C. A second version (with subscript IO, for “ice-only”) assumes that the radar reflectivity is dominated by the contribution from ice particles and does not attempt to estimate liquid water content below 0°C. This is consistent with assumptions in VarCloud and should provide a better comparison between the two products. It is also supported by observational evidence that  $Z_e$  is dominated by ice in mixed phase clouds (Hogan et al. 2003; Zuidema et al. 2005). Therefore, the ice-only CloudSat product rather than the standard version is used in this paper to compare IWC retrievals and will be referred to as “CloudSat ice-only”.

#### c. Empirical formula for IWC as a function of reflectivity and temperature

For empirical formulas relating IWC to  $Z_e$  using aircraft measurements, the size distribution is provided by the measurements and no assumptions on its shape need to be made. Hogan et al. (2006b) derived the following empirical relationship for the expected value of IWC as a function of 94 GHz radar reflectivity factor  $Z$  and temperature  $T$

$$\log_{10}(\text{IWC}) = 0.000580ZT + 0.0923Z - 0.00706T - 0.992, \quad (2)$$

which will be referred to as H06. Here, IWC is given in  $\text{g m}^{-3}$ ; radar reflectivity factor  $Z$  is in dBZ; and  $T$  in °C. The CloudSat products assume a different calibration for the 94 GHz radar than the empirical formulas  $\text{IWC}(Z, T)$ .

A conversion from the CloudSat observed  $Z_e$  to the  $Z$  in (2) is done by

$$Z_e = \frac{0.93}{|K_w(T_0)|^2} Z, \quad (3)$$

where 0.93 is the dielectric factor of liquid water at cm-wavelengths used in the empirical formulas  $IWC(Z,T)$  (Hogan et al. 2006b; Protat et al. 2007) and  $|K_w(T_0)|^2 = 0.75$  is the value used to calibrate the CloudSat radar, which is the dielectric factor of liquid water at 10°C at 94 GHz (Tanelli et al. 2008).

The formula (2) was derived using the Brown and Francis (1995) mass-diameter relationship and the Mie theory for radar scattering, which assumes that particles are modelled as spheres. Formulas such as (2) provide a best fit for  $IWC(Z,T)$  given the observations from which they are derived, which is a different approach from the VarCloud and CloudSat retrievals, even though the latter uses no more or less data than (2). The fractional error for IWC derived using (2) is +55%/−35% between −20°C and −10°C and +90%/−47% for  $T < -40^\circ\text{C}$  (Hogan et al. 2006b).

The inputs for the empirical formula (2) are the temperatures from ECMWF and the equivalent radar reflectivity factor  $Z_e$  from the CloudSat product 2B-GEOPROF, converted using (3). In this estimation of IWC the 2-way gas attenuation down to 0°C will be ignored, for this is typically less than 0.5 dB (Hogan and Illingworth 1999).

The formula  $IWC(Z,T)$  in (2) was derived using an aircraft measurement data set for northern hemisphere mid-latitudes only. Protat et al. (2007) evaluated this formula against data that included tropical cirrus and found that IWC estimates from (2) had fractional errors of +80% and −44% compared to the IWC calculated from the true size distribution. The  $IWC(Z,T)$ -relationship derived by Protat et al. (2007) for the global data set produced fractional errors of +69%/−41%. Since the *a priori* for VarCloud is derived from the same data set used by Protat et al. (2007), we will include their empirical formula in our comparison of the mean root-mean-squared (rms) difference between the different products. This relationship is

$$\log_{10}(\text{IWC}) = 0.000491ZT + 0.0939Z - 0.0023T - 0.84, \quad (4)$$

which will be referred to as P07. Similar to H06, this formula is derived using Mie theory for radar scattering in the non-Rayleigh regime. The Brown and Francis (1995) mass-diameter relationship is also applied, but using  $D_{\max}$  as the diameter rather than  $D_{\text{mean}}$ , which leads to an overestimate in IWC of about 50% (Hogan et al. 2010).

#### d. Standard MODIS product

MODIS measures reflectances at 36 wavelengths, including visible and near-infrared bands. For each cloudy pixel the MODIS retrieval determines the thermodynamic

phase (ice, liquid, mixed, uncertain), with the remainder of pixels flagged “clear” (King et al. 2004).

Ice-cloud optical depth  $\tau$  and mean effective radius  $\langle r_e \rangle$  in the MODIS products are derived through the best fit of the reflectance for a given observation to library calculations assuming plane-parallel homogeneous clouds (King et al. 1997). The ice reflectance library is generated from a database of 1117 ice particle size distributions from different field campaigns in the midlatitudes and in the tropics (Baum et al. 2005a). The reflectance functions are calculated at the MODIS visible and near-infrared wavelength bands for each size distribution and a range of optical thicknesses  $\tau$ , providing a look-up table for comparison with measured reflectance. Through a  $\chi^2$  test of the calculated reflectance and the measured reflectances, the combination of the size distribution and the optical thickness providing the best fit for all wavelength bands is retrieved.

The retrieval of  $\langle r_e \rangle$  through the use of radiometer observations is heavily weighted to the cloud top (McFarquhar and Heymsfield 1998; Platnick 2000). For instance in the near-infrared 2.2  $\mu\text{m}$  channel, using a radiative transfer code McFarquhar and Heymsfield (1998) argued that only the uppermost four or five optical depths of the cloud contribute to the reflectance. Therefore,  $\langle r_e \rangle$  retrievals for optically thick ice clouds will be dominated by particles near cloud top. In the retrieval of  $\tau$  and  $\langle r_e \rangle$ ,  $r_e$  and IWC are assumed constant with height, so that IWP is derived from optical thickness and  $\langle r_e \rangle$  (King et al. 2006), using

$$\text{IWP} = \frac{4}{3} \frac{\rho_{\text{ice}} \tau \langle r_e \rangle}{Q_{\text{ext}}(r_e/\lambda)}, \quad (5)$$

with  $Q_{\text{ext}}(r_e/\lambda)$  the extinction efficiency at the reference wavelength for  $\tau$  ( $\lambda = 0.66\mu\text{m}$ ).

### 3. Ice-cloud occurrence

Prior to a comparison of the different products by their retrieval of IWC, the radar and lidar are compared by the fraction of ice clouds that they observe. The VarCloud target classification contains a flag indicating whether the observation was made by radar, lidar, or both. This way, the cloud occurrence measured by the radar and lidar combined can easily be determined, as well as the fraction of that portion observed by a single instrument. This will give us a first estimate on the fraction of ice clouds missed by a single instrument (compare Stephens et al. (2008)).

We restrict ourselves to tropospheric ice clouds, that is ice cloud observed at temperatures below 0°C and located below the tropopause height, which is provided in the CALIPSO data set and determined by NASA’s Global Modeling and Assimilation Office as the first minimum above the surface of the function  $0.03T(p) - \log_{10} p$ , with pressure  $p$  between 550 and 40 hPa. This range will be referred to as the subzero troposphere. The ice-cloud occur-

rences presented should therefore be interpreted in relation to this subzero troposphere.

The data are gathered into bins of  $2^\circ$  latitude, indicated by  $\phi_k$ , with the extreme latitudes of a typical A-Train orbit at  $81.8^\circ$  north and south; occurrences that depend on temperature are binned per  $^\circ\text{C}$ , indicated by  $T_j$ ; and  $j$  and  $k$  are indices to the bins. The following probabilities are then calculated for each latitude and within the subzero troposphere:

- $\mathcal{P}_k(C \wedge T_j)$ : Probability of ice-cloud occurrence and temperature  $T_j$  at latitude  $\phi_k$ ;
- $\mathcal{P}_k(T_j)$ : Probability of temperature  $T_j$  at latitude  $\phi_k$ ;
- $\mathcal{P}_k(C | T_j)$ : Probability of ice-cloud occurrence given temperature  $T_j$  and at latitude  $\phi_k$ ,

where the “ $\wedge$ ” denotes a joint occurrence, the “ $|$ ” signifies a conditional probability, and “ $C$ ” is an ice-cloud observation as classified in VarCloud.

Using Bayes’ theorem, the ice-cloud occurrence for a given temperature is obtained from the observations as follows

$$\mathcal{P}_k(C | T_j) = \frac{\mathcal{N}_k(C \wedge T_j)}{\mathcal{N}_k(T_j)}, \quad (6)$$

where the “ $\mathcal{N}$ ” indicates the number of individual observations of the given temperature and/or cloud scene. These occurrences, shown in Figure 2(a–d), reveal a similar vertical structure of the zonal average as that which has been presented in previous studies that make use of CloudSat and/or CALIPSO data (Bodas-Salcedo et al. 2008; Mace et al. 2009; Wu et al. 2009). The distinction between radar-only, lidar-only, and radar-lidar observations, however, highlights the advantages of the combined product. The radar does not capture many of the optically thinner ice clouds at lower temperatures (usually higher altitudes) for which the lidar shows higher ice-cloud occurrence. On the other hand, the lidar signal is often extinguished before it reaches the melting layer and observes less than 5% ice-cloud occurrence per  $^\circ\text{C}$  for most temperatures warmer than  $-10^\circ\text{C}$  where the radar regularly observes more than 10% occurrence. The ice-cloud occurrence observed by both radar and lidar (Figure 2(d)) shows some of the cloud climatological features that can be expected for the month of July. The intertropical convergence zone has shifted on average about  $8^\circ$  north of the equator; a higher ice-cloud occurrence has formed in the southern polar region; and the descending branches of the Hadley cell result in lower ice-cloud occurrences at about  $30^\circ$  either side of the equator.

The very high ice-cloud occurrences at the coldest temperatures in Figure 2(d) are deceptive, which is indicated using the temperature layer depth, that is the variation of

height with temperature, given by

$$L_k(T_j) = \frac{\mathcal{N}_k(T_j)}{\mathcal{V}_k} \Delta z, \quad (7)$$

with  $\mathcal{V}_k$  the total number of vertical profiles at latitude  $\phi_k$  and  $\Delta z$  the VarCloud vertical resolution of 60m. Thus,  $L_k(T_j)$  has the dimensions  $\text{m } ^\circ\text{C}^{-1}$ , or the inverse of a lapse rate and low values of  $L_k(T_j)$  occur at the cold temperatures near the tropopause, where the lapse rate increases. When these cold temperatures do occur in the subzero troposphere, they tend to be associated with cloud as indicated by the relatively high occurrences. In the Antarctic, this combination of low temperature layer depth and high cloud occurrence could be due to poor determination of the polar tropopause (Zängl and Hoinka 2001) and subsequent inclusion of polar stratospheric clouds, whereas in the tropics it may be linked to overshooting convection.

In Figure 3, the probabilities  $\mathcal{P}_k(C \wedge T_j)$  and  $\mathcal{P}_k(C | T_j)$  (given by (6)) are averaged over the latitude bins to obtain the global ice-cloud occurrence. For each bin  $k$  the probability is weighted by the area  $A_k$  of a sphere between the appropriate latitudes, thus giving a larger weight to cloud occurrences in the tropics than at midlatitudes. To obtain a measure of volume,  $A_k$  is multiplied by the mean depth of the subzero troposphere per profile at latitude  $\phi_k$ , given by

$$\langle L_k \rangle = \sum_j L_k(T_j). \quad (8)$$

In addition, probabilities conditional on temperature  $T_j$  such as (6) are weighted by the temperature occurrence at that latitude given by  $\mathcal{P}_k(T_j)$ . The globally averaged probability of the ice-cloud occurrence conditional on the occurrence of  $T_j$ , is then calculated from (6) as

$$\mathcal{P}(C | T_j) = \frac{\sum_k A_k \langle L_k \rangle \mathcal{P}_k(T_j) \mathcal{P}_k(C | T_j)}{\sum_k A_k \langle L_k \rangle \mathcal{P}_k(T_j)}, \quad (9)$$

where the combined weight of area, mean number, and temperature occurrence appears in the denominator and the subscript  $k$  is dropped on the left-hand side to denote the global probability.

The globally averaged conditional ice-cloud occurrences in Figure 3(a) peak at temperatures colder than  $-70^\circ\text{C}$  when they include all lidar observations, similar to Figures 2(c–d). Assuming that the ice-cloud occurrence observed from all radar and lidar observations is the total ice-cloud occurrence, in Figure 3(a) the fraction of ice clouds observed coincidentally by both instruments reaches over 50% at temperatures between  $-30.0^\circ\text{C}$  and  $-48.0^\circ\text{C}$ , providing a large range of temperatures over which a combined radar-lidar ice-cloud retrieval is applicable. The radar detects at least 50% of the ice clouds observed by the combination of the two instruments at temperatures warmer than  $-51.0^\circ\text{C}$ , whilst the lidar detects over 50% at temperatures colder than  $-25.0^\circ\text{C}$ .

The global averages for the joint ice-cloud and temperature occurrence  $\mathcal{P}(C \wedge T_j)$  are shown in Figure 3(b). The weighted global average ice-cloud occurrence in the subzero troposphere can be obtained by integrating  $\mathcal{P}(C \wedge T_j)$  over temperature, which for July 2006 gives 13.3% for all radar and lidar observations. Using only observations where at least the lidar is available (lidar-only and radar-lidar) this reduces to 8.7% whereas for the radar (radar-only and radar-lidar) it is 8.8%. If we assume the combined product to give the “true” ice-cloud occurrence, we can conclude that radar and lidar observe 65.9% and 65.0% of tropospheric ice clouds, respectively, for July 2006, with 31.0% observed by both the radar and the lidar.

#### 4. Ice water content distribution versus temperature

The deviation between different ice water content (IWC) retrievals from radar or radar-and-lidar observations is studied in this section using the joint probability density distribution of IWC versus temperature.

Figure 4 displays the all-sky joint distribution of IWC versus temperature for CloudSat ice-only, H06 IWC( $Z, T$ ), and the VarCloud-OA retrievals. Probabilities are calculated for each latitude, temperature, and IWC bin as follows

$$\mathcal{P}_k(\text{IWC}_x \wedge T_j) = \frac{\mathcal{N}_k(\text{IWC}_x \wedge T_j)}{\mathcal{N}_k}, \quad (10)$$

with  $x$  denoting logarithmic bins for IWC. These probabilities are subsequently weighted by  $A_k$  and  $\langle L_k \rangle$  to obtain the globally averaged joint distributions of IWC versus  $T$ .

The contour plots in Figure 4 show several differences between the various products in terms of the joint probability distribution of IWC and  $T$ . First of all, the empirical formula of H06 given by (2) may be directly compared with the CloudSat ice-only retrieval as both products use only radar reflectivity and temperature to obtain IWC. At temperatures colder than  $-20^\circ\text{C}$  the two products show a similar distribution of IWC, disregarding the tail at lower IWC values beyond the CloudSat ice-only minimum IWC of  $10^{-6} \text{ kg m}^{-3}$ .

The complete VarCloud-OA IWC retrieval is shown in Figure 4(e), the distribution including all radar observations is shown in Figure 4(c), and the distribution including all lidar observations is shown in Figure 4(d). The inclusion of lidar observations extends the IWC distribution to higher occurrences at lower IWC values and colder temperatures compared to the radar-only retrievals in Figures 4(a), 4(b), and 4(c). Figures 4(f–h) show the IWC from VarCloud-OA where ice clouds are observed by (f) radar-only, (g) lidar-only, and (h) radar-and-lidar. In these panels, the H06 retrieval at the CloudSat sensitivity threshold of  $-28 \text{ dBZ}$  roughly separates the lidar-only IWC retrievals from the retrievals that include radar observations (dashed line). Instrument sensitivities to different ranges

of IWC emerge from these figures as the highest IWC are retrieved where only the radar is available. These occurrences are closest to the melting layer and are likely to be the furthest removed from cloud top, where the lidar signal will have been extinguished. The lowest IWC values are retrieved where only the lidar is available, for low IWC is associated with smaller ice particles, which do not lead to high enough reflectivities at 94 GHz beyond the CloudSat threshold of  $-28 \text{ dBZ}$ .

In Figures 4(a–e) we also show the in-cloud median and mean IWC versus temperature, that is the median and mean IWC for a given temperature only including values of  $\text{IWC} > 0$ . The domination of the in-cloud mean by the highest IWC values is apparent from Figure 5, which shows the cumulative in-cloud IWC distribution versus temperature. For all retrievals and at all temperatures, the in-cloud mean IWC lies between the 95th and 99th percentile. A comparison between the VarCloud retrieval for all (radar and/or lidar) observations with the CloudSat ice-only retrieval in Figure 5(a) reveals a similar distribution shape at temperatures warmer than  $-50^\circ\text{C}$ , but a shift towards lower in-cloud IWC percentiles for the VarCloud retrieval at colder temperatures due to the inclusion of lidar-only retrievals of IWC, as seen in Figure 4(g).

When the lidar-only retrievals are excluded from the VarCloud distribution in Figure 5(b), the CloudSat ice-only and VarCloud distributions are very similar for temperatures colder than  $-10^\circ\text{C}$  and between the 25th and 90th percentiles. The in-cloud means of the two distributions, however, still differ by up to a factor 4, indicating that the mean IWC is highly sensitive to the top 5% of the IWC distribution, which is where the mass-size relationships and radar scattering models are most uncertain. In radar retrievals, high IWC values are obtained only when high  $Z_e$  is observed. High  $Z_e$  involve non-Rayleigh scattering, which is treated differently by the retrievals as summarised in Table 1 and will result in differences in retrievals of high IWC. Ice-cloud radiation depends on the full IWC distribution and not just on the most optically thick ice clouds where the dependence of radiation on IWC has saturated. It is therefore important to report the full IWC probability distribution and not just the means, which are dominated only by the top 5% of IWC values.

The CloudSat ice-only IWC has its 95th and 99th percentiles at considerably lower IWC than the other retrievals, with the in-cloud mean deviating up to a factor 7 from VarCloud-OA in Figure 5(b). Austin et al. (2009) acknowledge possible violations in the CloudSat retrieval of their assumptions for large particle sizes that are generally associated with high  $Z_e$  values ( $Z_e > 20 \text{ dBZ}$ ), which may affect the high end of IWC values retrieved. The highest in-cloud mean IWC is retrieved by H06, followed by VarCloud-SA (“spherical aggregates”), with the H06 mean 50% higher than VarCloud-SA near the melting layer. The VarCloud-

OA and VarCloud-SA retrievals have very similar distributions, although the latter appears to retrieve consistently higher IWC, with the in-cloud mean up to 50% higher than VarCloud-OA.

## 5. Mean ratio between different ice water content retrievals

The discussion of the IWC distribution in the previous section focused on differences between IWC retrievals through their overall statistics. This section instead focuses on the statistics of the differences in IWC between simultaneous retrievals. This provides an additional comparison, whilst its results relate to the findings in the previous section.

For the purpose of this discussion, we set the “control” product to be H06 and define the logarithmic difference

$$\mathcal{D} = \ln \left[ \frac{\text{IWC}_R}{\text{IWC}_{\text{control}}} \right], \quad (11)$$

where “R” is one of VarCloud-OA, VarCloud-SA, CloudSat ice-only, or P07. The rms difference in  $\ln(\text{IWC})$  is then formulated as

$$\mathcal{S} = \sqrt{\langle \mathcal{D}^2 \rangle - \langle \mathcal{D} \rangle^2}. \quad (12)$$

Since the CloudSat products are on a 240 m grid as opposed to the 60 m grid for the VarCloud derived products,  $\mathcal{D}$  and  $\mathcal{S}$  are calculated only when both the CloudSat ice-only product retrieves  $\text{IWC} > 0$  and the products on the 60 m vertical grid retrieve  $\text{IWC} > 0$  at the vertical level nearest to the CloudSat level. To ensure a like-with-like comparison, statistics are only gathered when all products simultaneously retrieve  $\text{IWC} > 0$ , which effectively excludes VarCloud lidar-only retrievals. The means of (11) and (12) are gathered for each temperature  $T_j$  (per °C) and latitude  $\phi_k$  (per 2°) and subsequently weighted by  $A_k$ ,  $\langle L_k \rangle$ , and  $\mathcal{P}(T_j)$  following (9). In Figure 6 we then show the mean ratios in IWC, given by

$$\mathcal{R} = \exp\langle \mathcal{D} \rangle. \quad (13)$$

The variations with temperature of the mean ratio in IWC in Figure 6 relate more to the differences in the in-cloud median rather than the in-cloud mean of the IWC distributions in Figures 4 and 5. Although large differences between the in-cloud means appear in Figure 5, they will have a small impact on the mean ratio in retrieved IWC between products due to their low occurrence indicated by their location beyond the 90th percentiles. The mean ratio between the VarCloud-OA IWC retrieval and H06 is less than 1 at all temperatures, although it is within the rms difference from  $\mathcal{R} = 1$ . The slightly higher IWC retrievals from VarCloud-SA compared to VarCloud-OA in Figure 5(c) are echoed in Figure 6(a), where both products display a similar variation with temperature in their mean

ratios with respect to H06, but the VarCloud-SA mean ratio is consistently higher than the VarCloud-OA mean ratio.

The CloudSat ice-only mean ratio with respect to H06 in Figure 6(b) is larger than that for the VarCloud retrievals at most temperatures and exceeds  $\mathcal{R} = 1$  between  $-10^\circ\text{C}$  and  $-50^\circ\text{C}$ . The proximity of the CloudSat ice-only mean ratio with respect to H06 to  $\mathcal{R} = 1$  for temperatures warmer than  $-20^\circ\text{C}$  is surprising given the considerably different distributions displayed in Figure 4(a) and 4(b). However, the relatively large rms differences indicate a large spread of the IWC ratios between these two products.

The mean ratio variation with temperature shows a large difference between P07 and H06 in Figure 6(b). From the formulas for H06 and P07, given by (2) and (4), this difference appears from the coefficients for the temperature-only dependence, which are  $-0.00706$  and  $-0.0023$  respectively, both in units of  $\log_{10}(\text{kg m}^{-3}) \text{ } ^\circ\text{C}^{-1}$ . Accounting for the joint temperature-reflectivity coefficients in these formulas, for a fixed reflectivity, H06 will estimate IWC values that increase more rapidly as temperature decreases than P07 estimates of IWC. For the coldest temperatures, lower IWC with P07 could be due to the inclusion of tropical cirrus in its data set, whereas for warmer temperatures, higher IWC retrievals with P07 are likely due to the application of the Brown and Francis (1995) mass-diameter relationship with  $D_{\text{max}}$  rather than  $D_{\text{mean}}$ .

As with the ice-cloud occurrences shown in Figure 3, the mean ratios in IWC may depend on regional differences in ice-cloud distribution. In particular, H06 is derived from aircraft measurements in northern hemisphere midlatitudes, whereas P07 includes IWC distributions measured in the tropics. The mean ratio comparison between different latitude bands is provided in Figure 7 using H06 as the control. The mean ratios with respect to H06 look similar for all three regions at temperatures warmer than  $-50^\circ\text{C}$  where the radar observes at least 50% of the ice clouds used for the retrieval. For the southern hemisphere midlatitudes, however, the VarCloud-OA and VarCloud-SA mean ratios with respect to H06 have both increased at the coldest temperatures (below  $-50^\circ\text{C}$ ) compared to the other two regions. It should be noted that very little ice cloud is observed by the radar at these colder temperatures in general, but also that the aircraft measurements from which H06 has been derived do not contain any measurements from southern hemisphere midlatitudes. A similar comparison using P07 as the control showed no different behaviour from Figure 7 apart from the strong difference in temperature variation that is apparent from Figure 6(b) and is therefore not shown.

In Figure 8, the mean ratio in retrieved IWC given by (11) is shown with control H06, but now versus the radar reflectivity factor  $Z_e$ , which is obtained from the CloudSat

observations using (3). The mean ratio variation with reflectivity shows only a slight difference between the H06 and P07, as their coefficients for the reflectivity-only dependence in (2) and (4) are similar, namely 0.0923 and  $0.0939 \log_{10}(\text{kg m}^{-3}) \text{ dBZ}^{-1}$ . CloudSat ice-only and VarCloud show good agreement with H06 for lower reflectivities ( $Z_e < -10 \text{ dBZ}$ ) and are separated from a mean ratio of 1 with H06 within their mean rms differences. At these low reflectivities the CloudSat ice-only IWC retrieval has a maximum mean ratio of 1.5 compared to the VarCloud-OA retrieval.

Reflectivity dependence is shown for reflectivities up to 10 dBZ, for only few reflectivities larger than 10 dBZ occur in the data set from which H06 has been derived (Hogan et al. 2006b). At high reflectivities ( $Z_e > 0 \text{ dBZ}$ ), the VarCloud-SA product shows the best agreement with H06, which can be expected since both retrievals explicitly assume that all particles are spheres and they apply the same mass-size relationship. The VarCloud-OA product models ice particles as oblate spheroids for radar scattering, which in the non-Rayleigh scattering regime implies a lower IWC for the same reflectivity. This can be seen in Figure 8 as a shift to lower ratios compared to the VarCloud-SA ratios for higher reflectivities where non-Rayleigh scattering is likely to occur. The CloudSat ice-only product deviates from H06 most notably at these high reflectivities, which is likely due to the difference in treatment of non-Rayleigh scattering.

## 6. Vertically integrated ice-cloud properties

In this section, VarCloud profiles of IWC and  $\alpha_v$  are compared with MODIS retrievals of IWP and  $\tau$ , as well as  $\langle r_e \rangle$ , although some precautions are necessary to ascertain a like-with-like comparison.

Firstly, MODIS only retrieves cloud-ice properties for a 1 km observation pixel when it has determined an ice-cloud phase. The full cloud column is then assumed to consist of ice, so that the measured reflectances associated with the cloud column are attributed to ice-cloud optical depth and ice water path. VarCloud, however, can distinguish liquid clouds and rain underneath ice clouds and will only retrieve ice properties for the part of the cloud it determines to be ice-phase. Furthermore, profiles that only contain subvisual cirrus are likely to be detected as ice-only by VarCloud, but may be missed by MODIS. The occurrence of these possible mismatches in ice-cloud determination are summarised by their cumulative fraction of all profiles versus latitude for daytime observations in Figure 9. Only the fraction of profiles indicated by the solid black line in this figure (MODIS and VarCloud both determine ice-only cloud) will be used to generate the statistics in this section.

Secondly, MODIS estimates IWP from its  $\tau$  and  $\langle r_e \rangle$

retrievals using (5), where  $\langle r_e \rangle$  is dominated by the top 4 or 5 optical depths, so that any differences emerging from the IWP comparison may be due to the application of this method in contrast with the full IWC profile. This section will therefore include a comparison between IWP estimated using the MODIS method (5) with the VarCloud  $\tau$  and  $\langle r_e \rangle$ , the latter restricted to cloud top, and IWP obtained from the VarCloud IWC profiles.

Figure 10 shows the zonal mean of  $\tau$ ,  $\langle r_e \rangle$ , and IWP, for VarCloud-OA, VarCloud-BR, and MODIS, using only jointly observed ice-only values. A factor of 2 difference between MODIS and VarCloud-OA estimates of mean  $\tau$  is apparent throughout nearly all latitudes in Figure 10(a). Zhang et al. (2009) reported substantial differences between ice-cloud optical depth derived from MODIS and from POLDER (“POLARization and Directionality of the Earth’s Reflectances”), which is aboard another satellite in the A-Train constellation. The POLDER optical depths were found to be lower than MODIS with the mean ratio between the two products being 0.81. Adjusting the ice particle model to that used by the MODIS product (Baum et al. 2005a,b), a much better agreement of mean optical depth between the two products was achieved (Zhang et al. 2009). Similarly, a change in the VarCloud ice particle model affects the optical depth. To illustrate this, we consider the VarCloud-BR retrieval, which assumes a bullet rosette shape for ice particles instead of the Brown and Francis (1995) assumption in VarCloud-OA. This results in higher retrievals of the visible extinction coefficient  $\alpha_v$  with factors of 2 and higher differences in radar-only observations (Delanoë and Hogan 2010), which are most prevalent in deep ice clouds where the lidar signal is extinguished long before it reaches cloud base. Since the highest  $\tau$  retrievals from deep ice clouds dominate the zonal average, the change to the VarCloud-BR product leads to a closer match with the MODIS average in Figure 10(a). The VarCloud-BR product is introduced in this section to stress the sensitivity of ice-cloud retrievals to the ice particle model, not as a more appropriate method than VarCloud-OA. Indeed, the assumption of bullet rosettes throughout the ice-cloud profile would not provide a good fit to radar observations from H06 in the temperature range from 0 to  $-40^\circ\text{C}$ , while Brown and Francis (1995) performed very well (Hogan et al. 2006b).

The VarCloud microphysical model consists of the Brown and Francis (1995) mass-diameter relationship. Particle size can be described by the effective radius (Foot 1988), given by

$$r_e = \frac{3}{2} \frac{\text{IWC}}{\rho_{\text{ice}} \alpha_v}, \quad (14)$$

where  $\rho_{\text{ice}} = 917 \text{ kg m}^{-3}$  is the density of ice. VarCloud-BR IWC and  $\alpha_v$  retrievals are affected differently by the new ice particle assumption, depending on whether the retrieval includes radar and/or lidar observations. How-

ever, from the direct comparison between VarCloud-OA and VarCloud-BR retrievals of IWC and  $\alpha_v$  by Delanoë and Hogan (2010), and using (14), lower  $r_e$  retrievals can be expected from VarCloud-BR compared to VarCloud-OA. Indeed, this difference between the two VarCloud  $r_e$  retrievals appears from the zonal averages of mean effective radii in Figure 10(b). The VarCloud-BR zonal average of  $\langle r_e \rangle$  is comparable to the MODIS average in the tropics, but they differ by a factor of 2 or higher for the midlatitudes. The VarCloud-OA zonal average of  $\langle r_e \rangle$  appears to be consistently about  $10\mu\text{m}$  higher than the VarCloud-BR retrieval.

The differences between the products observed for the in-cloud zonal averages of  $\tau$  and  $\langle r_e \rangle$  do not simply translate to the IWP comparison of Figure 10(c). From the MODIS IWP retrieval (5) one may expect that the good match between the VarCloud-BR and MODIS retrievals of  $\langle r_e \rangle$  and  $\tau$ , particularly in the tropics, would lead to a similarly good comparison between the two for IWP. However, the VarCloud-BR in-cloud zonal average of IWP, calculated from the integral of IWC with height, is higher than the MODIS average with typically a factor 2–4 difference in the tropics. VarCloud-OA instead provides good agreement with MODIS in Figure 10(c), despite the poor agreement in  $\tau$  and  $\langle r_e \rangle$ .

Differences between products as observed through the zonal averages of Figure 10 cannot immediately be attributed to instrument and algorithm sensitivities. Figures 11(a–f) display histograms of joint probability distributions of  $\tau$ ,  $\langle r_e \rangle$ , and IWP between MODIS and either VarCloud-OA or VarCloud-BR. The shape of the distribution in Figure 11(a) is aligned with a fixed ratio between the MODIS and VarCloud-OA retrievals of  $\tau$ , with peak occurrences indicating that MODIS  $\tau$  are consistently a factor 2 higher than VarCloud-OA, which explains the difference in zonal mean  $\tau$  from Figure 10(a). For VarCloud-BR, the peak occurrences in the joint distribution in Figure 11(b) spread from retrievals of  $\tau$  that are a factor 2 lower than MODIS to retrievals a factor 2 higher than MODIS. This indicates that a cancellation of difference in retrievals of high  $\tau$  has led to a reasonable agreement in zonal mean  $\tau$  in Figure 10(a). Differences in high  $\tau$  retrievals between the two VarCloud products is consistent with the differences in  $\alpha_v$  for radar-only retrievals illustrated by Delanoë and Hogan (2010). The joint distribution of the VarCloud and MODIS  $\tau$  retrievals shows a larger tail towards higher  $\tau$  for VarCloud-BR compared to VarCloud-OA, whereas at the low  $\tau$  end — where radar-only retrievals are less likely — the two joint distributions show a similar spread.

A direct comparison between MODIS and the VarCloud retrievals of  $\langle r_e \rangle$  does not provide a consistent difference between the products in Figures 11(c), and 11(d) that can explain the differences in zonal averages from Figure 10(b). For VarCloud-BR, the joint distribution with MODIS of

individual  $\langle r_e \rangle$  retrievals has its peak stretched towards a ratio of 1 between the two products in Figure 11(d) compared to the distribution with VarCloud-OA in Figure 11(c), but the overall shape of the distributions indicate a tendency of MODIS retrievals to lie between  $20\mu\text{m}$  and  $40\mu\text{m}$ , whereas both VarCloud products regularly retrieve  $\langle r_e \rangle$  above  $50\mu\text{m}$ . MODIS retrievals of  $\langle r_e \rangle$  are dominated by cloud top, yet a restriction of VarCloud  $\langle r_e \rangle$  to the top 5 ice-cloud optical depths leads to a slight improvement only for large  $\langle r_e \rangle$  (not shown), whilst the shape of the distribution of joint  $\langle r_e \rangle$  remains similar to that in Figures 11(c) and (d), hence the sensitivity to cloud top does not explain the basic difference between the two retrievals.

The differences in zonal averages of IWP in Figure 10(c) are reflected in the joint distributions of IWP retrievals between MODIS and the VarCloud retrievals in Figures 11(e) and (f). The VarCloud-OA joint distribution with MODIS IWP in Figure 11(e) is centered around a ratio of 1, with slightly higher MODIS retrievals of low IWP, which do not contribute much to the zonal averages. Interestingly, the VarCloud-BR IWP distribution stretches to lower values than VarCloud-OA. VarCloud-BR generally retrieves lower IWC values compared to VarCloud-OA for lidar-only observations of ice cloud (Delanoë and Hogan 2010), so that cloud observed completely by the lidar, will have a lower IWP retrieval from VarCloud-BR compared to a VarCloud-OA IWP retrieval. Peak occurrences in the joint distribution of MODIS IWP with VarCloud-BR now appear at higher values than for VarCloud-OA, where VarCloud-BR IWP is more than a factor 2 higher than MODIS, which explains the higher zonal averages for VarCloud-BR in Figure 10(c).

For the VarCloud retrievals it is possible to derive IWP from  $\tau$  and  $\langle r_e \rangle$  using (5), simulating the method used by MODIS. For liquid water clouds in the boundary layer, a similar method to (5) exists to derive liquid water path from optical depth and effective radius (derived from cloud top), but an adjusted model is used to account for variations of liquid water content and effective radius with height (Wood and Hartmann 2006). Such adjustments for ice clouds to (5) could improve the IWP comparison between MODIS and VarCloud, and in Figures 11(g) and (h) we show the difference between a retrieval using (5) and IWP as the integral of IWC, both from VarCloud profiles only, to investigate whether this difference in IWP retrieval method can explain the differences in IWP seen in Figures 11(e) and (f). When applying (5) with  $Q_{\text{ext}} = 2$ ,  $\langle r_e \rangle$  is restricted to  $r_e$  retrievals from the top 5 optical depths of ice clouds, whilst  $\tau$  is restricted to a maximum value of 100 as in the MODIS retrievals, thus applying the MODIS sensitivity restrictions. Both VarCloud retrievals show that for  $\tau$  up to about 10, the two methods for IWP retrieval agree with a mean ratio that is within one rms difference of 1. The IWP method using (5) retrieves on average lower

values than the integral over IWC for  $\tau$  larger than 10, reaching a mean factor of 2 or larger difference between the two methods once  $\tau$  exceeds 100. Such retrievals are associated with deep ice clouds, where  $r_e$  can range from 10  $\mu\text{m}$  at cloud top to 80  $\mu\text{m}$  near the melting layer, so that a restriction of  $\langle r_e \rangle$  retrieval to the top of the cloud leads to an underestimate of the IWP contribution from the lower part of the cloud. The assumption in the IWP estimate using (5) of ice-cloud profiles with constant  $r_e$  breaks down when cloud-ice properties vary over a wide range of scales within the profile, which follows from the inequality below

$$\begin{aligned} \text{IWP} &= \sum [\text{IWC} \times \Delta z] = \frac{2}{3} \rho_{\text{ice}} \sum [r_e \alpha_v \times \Delta z] \quad (15) \\ &\neq \frac{2}{3} \rho_{\text{ice}} \langle r_e \rangle \tau . \end{aligned}$$

Thus, for  $\tau > 10$ , the difference in IWP retrieval methods explains the difference in high IWP estimates seen in Figures 11(e) and (f) and consequently the large differences in zonal mean IWP in Figure 10(c). For thin ice clouds, however, the differences in Figures 11(e) and (f) for low IWP estimates are not explained by the difference in IWP retrieval methods, for  $\langle r_e \rangle$  is a better characterization of mean particle size for the full cloud-ice column and Figures 11(g) and (h) show that the two methods agree well.

## 7. Conclusions

A combined radar-lidar cloud-ice retrieval using CloudSat and CALIPSO measurements (Delanoë and Hogan 2010), VarCloud, has been compared with coincident cloud-ice retrievals from the A-Train satellites. The advantages of a multi-instrument algorithm have been illustrated by the larger fraction of ice cloud observed by the combination of radar and lidar compared to the single instruments, as well as the greater range of IWC values obtained due to the different sensitivities of each instrument.

The radiative impact of ice clouds depends on their full IWC distribution, not just the mean or integrated values (IWP), which will be weighted by the most optically thick (parts of the) ice clouds. The retrievals that provide IWC profiles have been shown to produce similar IWC distributions with temperature, with typical differences of the in-cloud median IWC at less than 50%. Factors of 2–7 difference in mean IWC values between the retrievals were shown to be dominated by retrievals of high IWC with low occurrence, due to differences between the methods in the treatment of non-Rayleigh scattering for observations of high  $Z_e$ . Further evaluation of radar scattering models with in situ measurements will be necessary to constrain high IWC values.

Retrievals from passive and active satellite observations were compared using MODIS and VarCloud for joint observations with ice-only cloud profiles. A change in the VarCloud ice particle model did not explain the large spread

in the joint distribution of  $\langle r_e \rangle$ . A restriction of VarCloud retrievals of  $\langle r_e \rangle$  to the top 5 optical depths of ice cloud reduced the occurrence of high  $\langle r_e \rangle$ , but again had no impact on the large spread of the distribution. The IWP comparison of MODIS with VarCloud-BR indicated a larger spread in IWP from the latter retrieval, which was explained by underestimates of IWC for lidar-only observations and overestimates for radar-only observations when bullet rosettes are used compared to oblate aggregates. A direct comparison of different IWP retrieval methods using the VarCloud profiles showed that an IWP retrieval using  $\tau$  and  $\langle r_e \rangle$  was in good agreement with the IWC profile for  $\tau < 10$ , but was reduced by a factor of 2 or more when  $\tau > 100$ .

The sensitivity of VarCloud to its ice particle model indicated that these assumptions partly explain differences with MODIS retrievals, whereas differences in IWP for high  $\tau$  were also affected by the IWP retrieval method. The poor agreement in  $\langle r_e \rangle$  between MODIS and VarCloud indicated a large uncertainty for this variable arising from the satellite and algorithm sensitivities, with MODIS assuming a constant multiple-habit ice particle distribution throughout the profile, determined by particle size measurements near the cloud top; and VarCloud assuming a single-habit ice particle distribution with sizes that may vary throughout the cloud column. The lack of agreement in  $\langle r_e \rangle$  for thin ice cloud, where MODIS reflectances can be assumed to come from the entire cloud column and where the MODIS IWP retrieval method for VarCloud shows good agreement with the full IWC profile, indicated that further cross-validation of these satellite retrievals requires a greater flexibility to test with different ice particle models within each algorithm.

### *Acknowledgments.*

We thank the ICARE Data and Services Center for their assistance, development support, and data processing for the VarCloud product. CALIPSO lidar data used are available at eosweb.larc.nasa.gov. The official CloudSat data products are available at cloudsat.cira.colostate.edu and are provided by the NASA CloudSat project. MODIS products are available online at modis-atmos.gsfc.nasa.gov and are provided by the MODIS Science Team.

## REFERENCES

- Anselmo, T., et al., 2006: Cloud Aerosol LIDAR Infrared Pathfinder Satellite Observations (CALIPSO). Data management system and data products catalog, CALIPSO documentation, NASA. Release 2.3, Document No: PC-SCI-503.
- Austin, R. T., A. J. Heymsfield, and G. L. Stephens, 2009:

- Retrieval of ice cloud microphysical parameters using the CloudSat millimeter-wave radar and temperature. *J. Geophys. Res.*, **114**, D00A23.
- Baum, B. A., A. J. Heymsfield, P. Yang, and S. T. Bedka, 2005a: Bulk scattering properties for the remote sensing of ice clouds. Part I: Microphysical data and models. *J. Appl. Meteorol.*, **44**, 1885–1895.
- Baum, B. A., P. Yang, A. J. Heymsfield, S. Platnick, M. D. King, Y.-X. Hu, and S. T. Bedka, 2005b: Bulk scattering properties for the remote sensing of ice clouds. Part II: Narrowband models. *J. Appl. Meteorol.*, **44**, 1896–1911.
- Benedetti, A., G. L. Stephens, and J. M. Haynes, 2003: Ice cloud microphysics retrievals from millimeter radar and visible optical depth using an estimation theory approach. *J. Geophys. Res.*, **108** (D11).
- Bodas-Salcedo, A., M. J. Webb, M. E. Brooks, M. A. Ringer, K. D. Williams, S. F. Milton, and D. R. Wilson, 2008: Evaluating cloud systems in the Met Office global forecast model using simulated CloudSat radar reflectivities. *J. Geophys. Res.*, **113**, D00A13.
- Brown, P. R. A. and P. N. Francis, 1995: Improved measurements of the ice water content in cirrus using a total-water probe. *J. Atmos. Ocean. Tech.*, **12**, 410–414.
- Delanoë, J. and R. J. Hogan, 2008: A variational scheme for retrieving ice cloud properties from combined radar, lidar, and infrared radiometer. *J. Geophys. Res.*, **113**(D0) (7204).
- Delanoë, J. and R. J. Hogan, 2010: Combined CloudSat-CALIPSO-MODIS retrievals of the properties of ice clouds. *J. Geophys. Res.* (*in press*).
- Delanoë, J., A. Protat, J. Testud, D. Bouniol, A. J. Heymsfield, A. Bansemer, P. R. A. Brown, and R. M. Forbes, 2005: Statistical properties of the normalized ice particle size distribution. *J. Geophys. Res.*, **110**, D10 201.
- Donovan, D. P., et al., 2001: Cloud effective particle size and water content profile retrievals using combined radar and lidar observations: 2. Comparison with IR radiometer and in situ measurements of ice clouds. *J. Geophys. Res.*, **106**, 27 449–27 464.
- Foot, J. S., 1988: Some observations of the optical properties of clouds – 2. Cirrus. *Q. J. R. Meteorol. Soc.*, **114**, 145–164.
- Francis, P. N., P. Hignett, and A. Macke, 1998: The retrieval of cirrus cloud properties from aircraft multispectral reflectance measurements during EUCREX’93. *Q. J. R. Meteorol. Soc.*, **124**, 1273–1291.
- Heymsfield, A. J., et al., 2008: Testing IWC retrieval methods using radar and ancillary measurements with in situ data. *J. Appl. Met. Clim.*, **47**, 135–163.
- Hogan, R. J., 2006: Fast approximate calculation of multiply scattered lidar returns. *Appl. Opt.*, **45**, 5984–5992.
- Hogan, R. J., D. P. Donovan, C. Tinel, M. A. Brooks, A. J. Illingworth, and J. P. V. P. Baptista, 2006a: Independent evaluation of the ability of spaceborne radar and lidar to retrieve the microphysical and radiative properties of clouds. *J. Atmos. Ocean. Tech.*, **23**, 211–227.
- Hogan, R. J., P. N. Francis, H. Flentje, A. J. Illingworth, M. Quante, and J. Pelon, 2003: Characteristics of mixed-phase clouds. I: Lidar, radar and aircraft observations from CLARE’98. *Q. J. R. Meteorol. Soc.*, **129**, 2089–2116.
- Hogan, R. J. and A. J. Illingworth, 1999: The potential of spaceborne dual-wavelength radar to make global measurements of cirrus clouds. *J. Atmos. Ocean. Tech.*, **16**, 518–531.
- Hogan, R. J., M. P. Mittermaier, and A. J. Illingworth, 2006b: The retrieval of ice water content from radar reflectivity factor and temperature and its use in evaluating a mesoscale model. *J. Appl. Meteorol.*, **45**, 301–317.
- Hogan, R. J., L. Tian, P. R. A. Brown, C. D. Westbrook, and J. D. Eastment, 2010: Radar scattering from ice aggregates using the horizontally aligned oblate spheroid approximation. *J. Appl. Met. Clim.* (*to be submitted*).
- Intrieri, J. M., G. L. Stephens, W. L. Eberhart, and T. Uttal, 1993: A method for determining cirrus cloud particle sizes using lidar and radar backscatter techniques. *J. Appl. Meteorol.*, **32**, 1074–1082.
- King, M. D., S. Platnick, P. A. Hubanks, G. T. Arnold, E. G. Moody, G. Wind, and B. Wind, 2006: Collection 005 change summary for the MODIS cloud optical property (06\_OD) algorithm. [Accessed via [http://modis-atmos.gsfc.nasa.gov/products\\_C005update.html](http://modis-atmos.gsfc.nasa.gov/products_C005update.html)], NASA. Version 3.1 (9 May 2006).
- King, M. D., S. Platnick, P. Yang, G. T. Arnold, M. A. Gray, J. C. Riedi, S. A. Ackerman, and K.-N. Liou, 2004: Remote sensing of liquid water and ice cloud optical thickness and effective radius in the Arctic: Application of airborne multispectral MAS data. *J. Atmos. Ocean. Tech.*, **21**, 857–875.
- King, M. D., S.-C. Tsay, S. E. Platnick, M. Wang, and K. N. Liou, 1997: Cloud retrieval algorithms for MODIS: Optical thickness, effective particle radius, and thermodynamic phase. MODIS algorithm theoretical basis document, NASA. ATBD-MOD-05.

- Mace, G. G., 2004: Level 2 GEOPROF product process description and interface control document (v.3). Tech. rep., CIRA, Colorado State University.
- Mace, G. G., Q. Zhang, M. Vaughn, R. Marchand, G. Stephens, C. Trepte, and D. Winker, 2009: A description of hydrometeor layer occurrence statistics derived from the first year of merged CloudSat and CALIPSO data. *J. Geophys. Res.*, **114**, D00A26.
- McFarquhar, G. M. and A. J. Heymsfield, 1998: The definition and significance of an effective radius for ice clouds. *J. Atmos. Sci.*, **55**, 2039–2041.
- Mitchell, D. L., 1996: Use of mass-and area-dimensional power laws for determining precipitation particle terminal velocities. *J. Atmos. Sci.*, **53**, 1710–1723.
- Mitrescu, C., J. M. Haynes, G. L. Stephens, S. D. Miller, G. M. Heymsfield, and M. J. McGill, 2005: Cirrus cloud optical, microphysical, and radiative properties observed during the CRYSTAL-FACE experiment. *J. Geophys. Res.*, **110** (D09208).
- Okamoto, H., S. Iwasaki, M. Yasui, H. Horie, H. Kuroiwa, and H. Kumagai, 2003: An algorithm for retrieval of cloud microphysics using 95-GHz cloud radar and lidar. *J. Geophys. Res.*, **108**(D7) (4226).
- Platnick, S., 2000: Vertical photon transport in cloud remote sensing problems. *J. Geophys. Res.*, **105** (D18), 22919–22935.
- Platnick, S., M. D. King, S. A. Ackerman, W. P. Menzel, B. A. Baum, J. C. Riédi, and R. A. Frey, 2002: The MODIS cloud products: Algorithms and examples from Terra. *IEEE Trans. Geosci. Remote Sens.*, **41** (2), 459–473.
- Protat, A., J. Delanoë, D. Bouniol, A. J. Heymsfield, A. Bansemmer, and P. Brown, 2007: Evaluation of ice water content retrievals from cloud radar reflectivity and temperature using a large airborne in site microphysical database. *J. Appl. Met. Clim.*, **46**, 557–572.
- Rodgers, C. D., 2002: *Inverse methods for atmospheric sounding: Theory and practice*. World Sci., Hackensack, N. J.
- Stephens, G. L., S.-C. Tsay, P. W. Stackhouse, and P. J. Flatau, 1990: The relevance of microphysical and radiative properties of cirrus clouds to climate and climate feedback. *J. Atmos. Sci.*, **47** (14), 1742–1753.
- Stephens, G. L., et al., 2002: The CloudSat mission and the A-Train. *Bull. Amer. Meteor. Soc.*, **83**, 1771–1790.
- Stephens, G. L., et al., 2008: CloudSat mission: Performance and early science after the first year of operation. *J. Geophys. Res.*, **113** (D00A18).
- Tanelli, S., S. L. Durden, E. Im, K. S. Pak, D. G. Reinke, P. Partain, J. M. Haynes, and R. T. Marchand, 2008: CloudSat’s cloud profiling radar after two years in orbit: Performance, calibration, and processing. *IEEE Trans. Geosci. Remote Sens.*, **46** (11), 3560–3573.
- Tinel, C., J. Testud, R. J. Hogan, A. Protat, J. Delanoë, and D. Bouniol, 2005: The retrieval of ice cloud properties from cloud radar and lidar synergy. *J. Appl. Meteorol.*, **44**, 860–875.
- Waliser, D. E., et al., 2009: Cloud ice: A climate model challenge with signs and expectations of progress. *J. Geophys. Res.*, **114**, D00A21.
- Warren, S. G. and C. J. Hahn, 2002: Clouds / Climatology. *Encyclopedia of the Atmospheric Sciences*, Academic Press.
- Winker, D. M., J. Pelon, and M. P. McCormick, 2003: The calipso mission: Spaceborne lidar for observation of aerosols and clouds. *Proc. SPIE Int. Soc. Opt. Eng.*, **4893**, 1–11.
- Wood, R. and D. L. Hartmann, 2006: Spatial variability of liquid water path in marine low cloud: The importance of mesoscale cellular convection. *J. Clim.*, **19**, 1748–1764.
- Wu, D. L., et al., 2009: Vertical distributions and relationships of cloud occurrence frequency as observed by MISR, AIRS, MODIS, OMI, CALIPSO, and CloudSat. *Geophys. Res. Lett.*, **36**, L09821.
- Zängl, G. and P. K. Hoinka, 2001: The tropopause in the polar regions. *J. Clim.*, **14**, 3117–3139.
- Zhang, Z., P. Yang, G. Kattawar, J. Riedi, L. C.-Labonnote, B. A. Baum, S. Platnick, and H.-L. Huang, 2009: Influence of ice particle model on satellite ice cloud retrieval: Lessons learned from MODIS and POLDER cloud product comparison. *Atmos. Chem. Phys.*, **9**, 7115–7129.
- Zuidema, P., et al., 2005: An Arctic springtime mixed-phase cloudy boundary layer observed during SHEBA. *J. Atmos. Sci.*, **62**, 160–176.

Product	Mass-area-size relationship	Radar scattering model	Particle size distribution
VarCloud-OA (Delanoë and Hogan 2010)	Aggregates	Oblate spheroids (T-matrix)	“Normalised”
VarCloud-SA	Aggregates	Spheres (Mie scattering)	“Normalised”
VarCloud-BR	Bullet rosettes	Spheres (Mie scattering)	“Normalised”
Formula IWC( $Z, T$ ) (Hogan et al. 2006b; Protat et al. 2007)	Aggregates	Spheres (Mie scattering)	Fit to aircraft distributions
CloudSat IWC (Austin et al. 2009)	Equivalent volume	Spheres (Parameterized Mie)	Lognormal
MODIS IWP (King et al. 2006)	Habit mixture	N/A	Gamma distribution

TABLE 1. A summary of the products used for comparison and their ice particle assumptions for calculating scattering properties. Products with “aggregates” make use of the Brown and Francis (1995) mass-diameter relationship and Francis et al. (1998) area-size relationship. “Habit mixture” stands for size-dependent distributions of plates, hollow columns, bullet rosettes, and aggregates as formulated by Baum et al. (2005a). “Bullet rosettes” employs the Mitchell (1996) mass-area-size relationship. “Equivalent volume” assumes the equivalent spherical volume for the ice crystal (Stephens et al. 1990). The radar scattering model is most relevant to retrievals with high  $Z_e$  and relates to the shape assumption for large particles in the non-Rayleigh scattering regime. For the CloudSat product, “Parameterized Mie” uses Mie theory with a correction factor and is derived from Benedetti et al. (2003). The “normalised” size distribution used in the VarCloud retrievals is described in Delanoë et al. (2005).

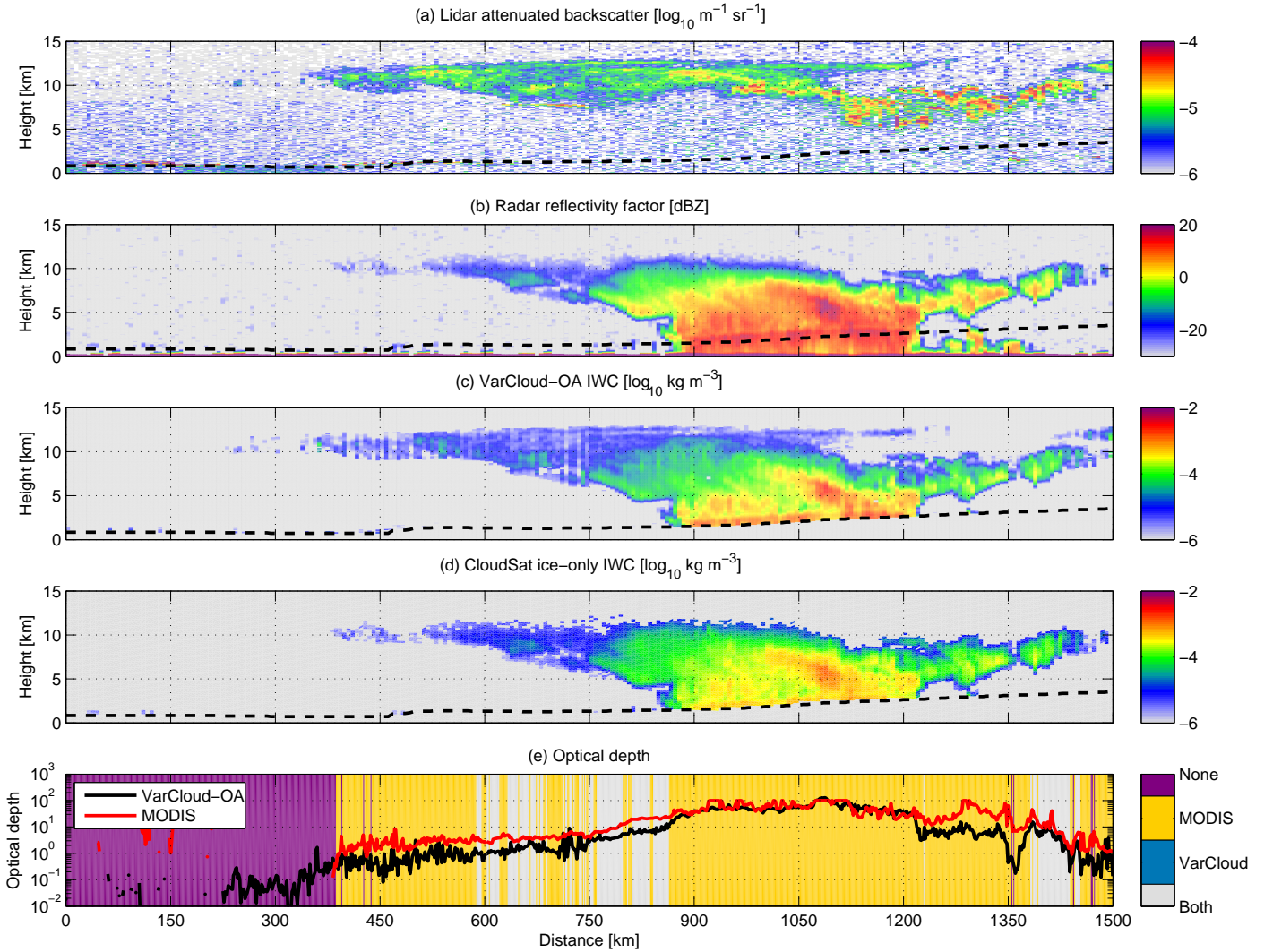


FIG. 1. CloudSat observations from orbit 01126 and collocated MODIS and CALIPSO data, 14th July 2006, 16:36:23–16:39:04 UTC. (a) Attenuated backscatter coefficient observed by the lidar. (b) Radar reflectivity factor  $Z_e$  observed by the CloudSat radar. (c) IWC retrieved by VarCloud-OA. (d) IWC from the CloudSat ice-only product. (e) Optical depth retrieved by VarCloud-OA (black) and MODIS (red), with coloured shading indicating which product has determined the profile to contain only ice. (a–d) Dashed line shows the height of  $T_w = 0^\circ\text{C}$  from the ECMWF modelled temperatures.

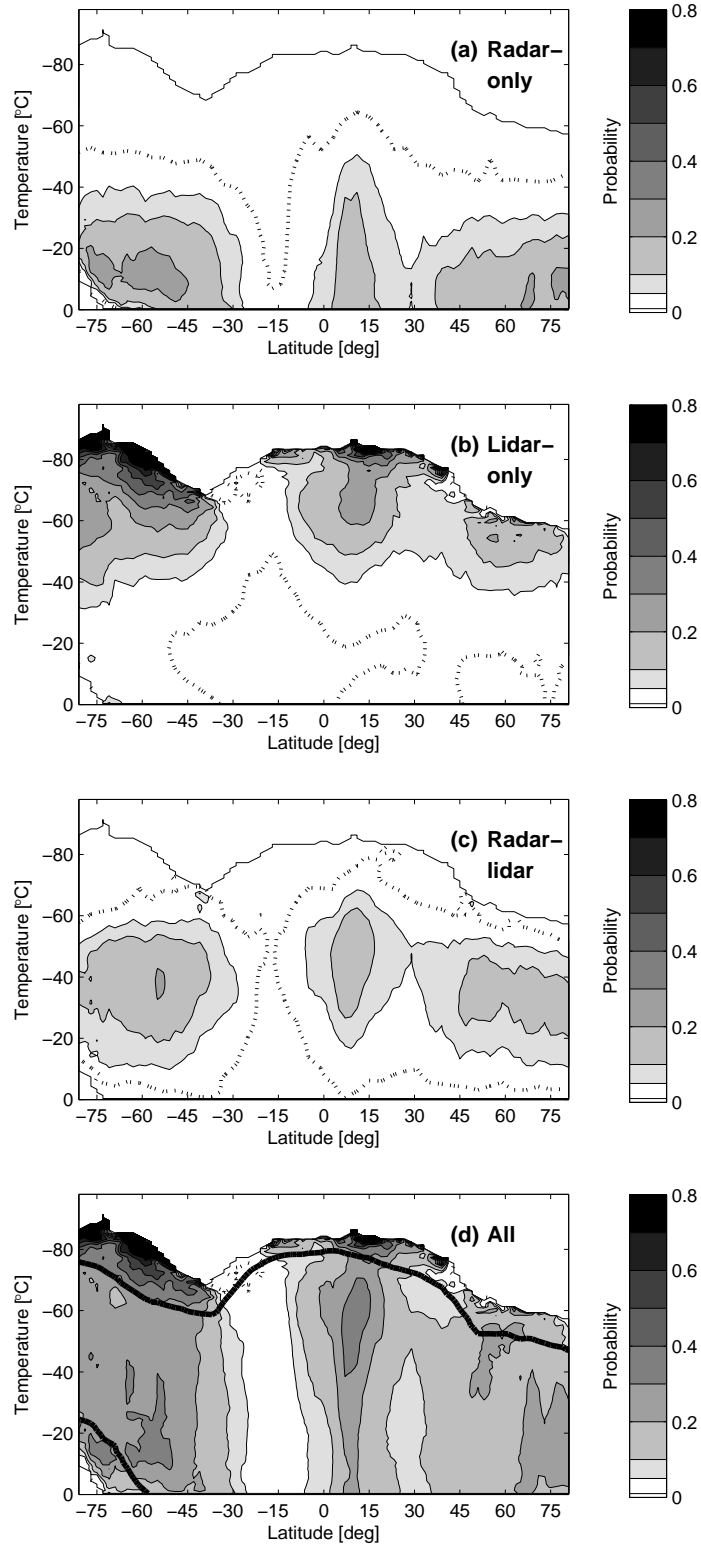


FIG. 2. (a–d) Probability of observing ice cloud in the subzero troposphere for a given temperature  $T_j$  and latitude  $k$ , i.e.  $\mathcal{P}_k(C | T_j)$ , for (a) radar-only, (b) lidar-only, (c) radar and lidar together, and (d) either radar or lidar or both. Thick lines in (d) indicate the  $90 \text{ m } ^\circ\text{C}^{-1}$  contour for temperature occurrence derived using (7), thereby indicating where the sample is small and the results may be less reliable. Broken lines show the 0.01 probability contour. Data are from July 2006.

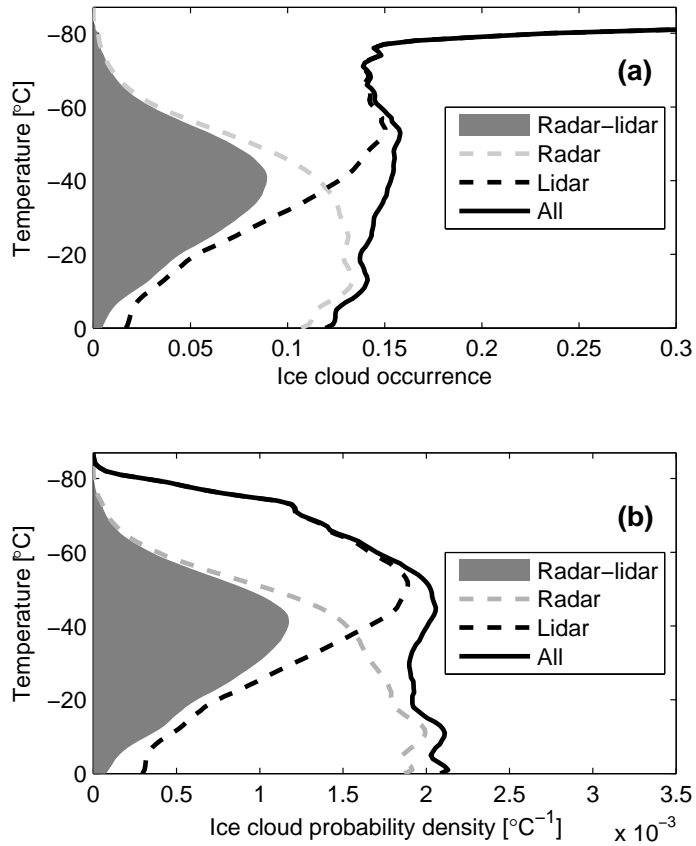


FIG. 3. (a) Ice-cloud occurrence versus temperature  $T_j$ , that is  $\mathcal{P}(C | T_j)$ , for different instrument combinations. These graphs can be interpreted as the average of ice-cloud occurrence in Figure 2(a–d) weighted by latitude. (b) Global distribution of ice clouds and temperature  $T_j$  between the melting layer and the tropopause, that is  $\mathcal{P}(C \wedge T)$ . This can be interpreted as a weighted average of Figure 2(a–d), multiplied by  $\mathcal{P}(T_j)$ . “Radar” implies where the radar detects ice cloud (Figures 2(a) and 2(c)); “lidar” implies where the lidar detects ice cloud (Figures 2(b) and 2(c)). Data are from July 2006.

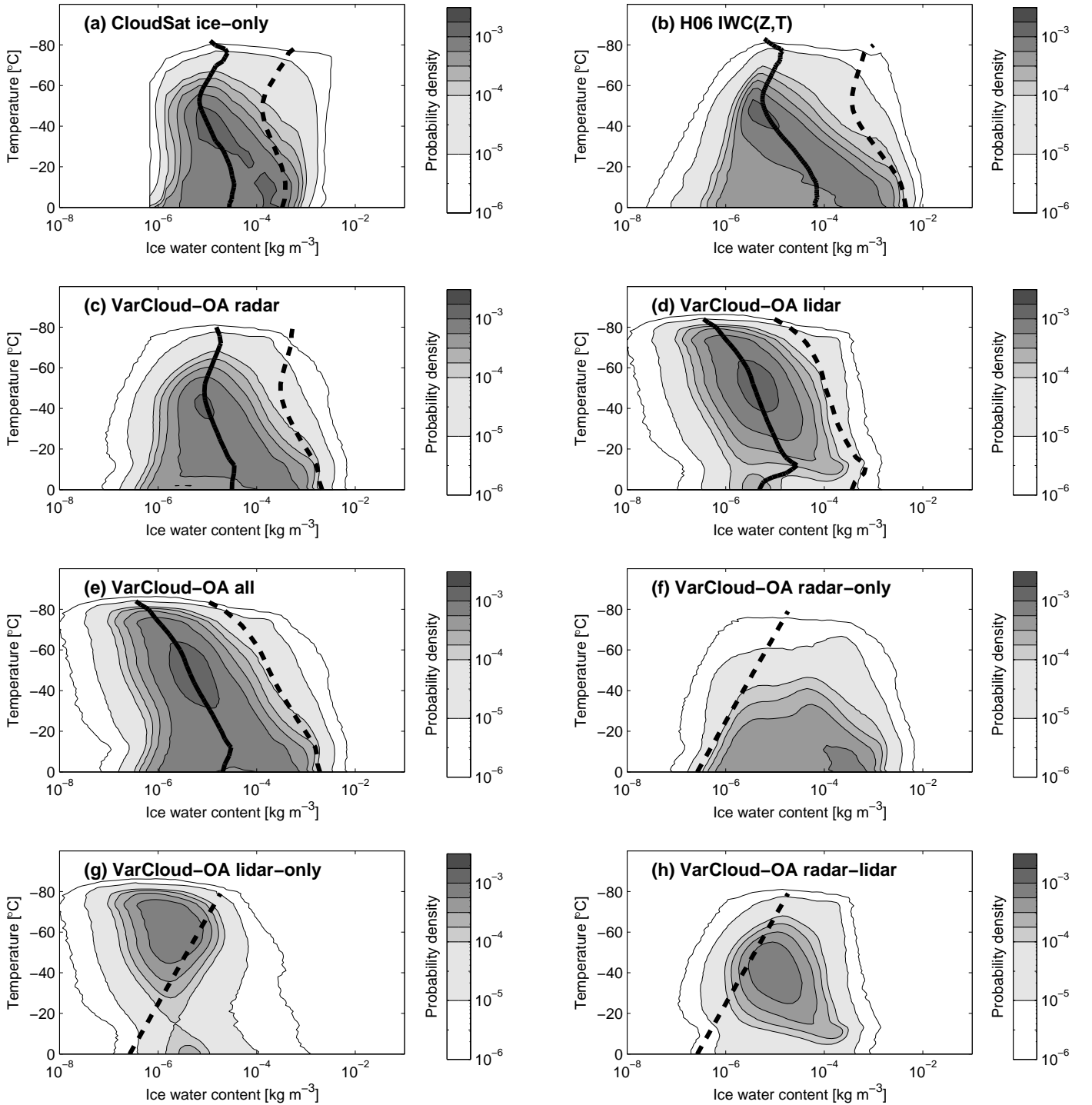


FIG. 4. IWC versus  $T$  frequency distribution for all skies, that is  $\mathcal{P}(\text{IWC}_x \wedge T_j)$ . Values are weighted averages over orbits and latitudes and are represented as the probability density per  $^{\circ}\text{C}$  per  $\log_{10}(\text{kg m}^{-3})$ . For (a–e) we also show the in-cloud median (solid) and weighted mean (dashed) IWC at each temperature. For (f–h) the dashed line indicates the IWC retrieved by H06 at the CloudSat sensitivity threshold of  $-28$  dBZ. Data are from July 2006.

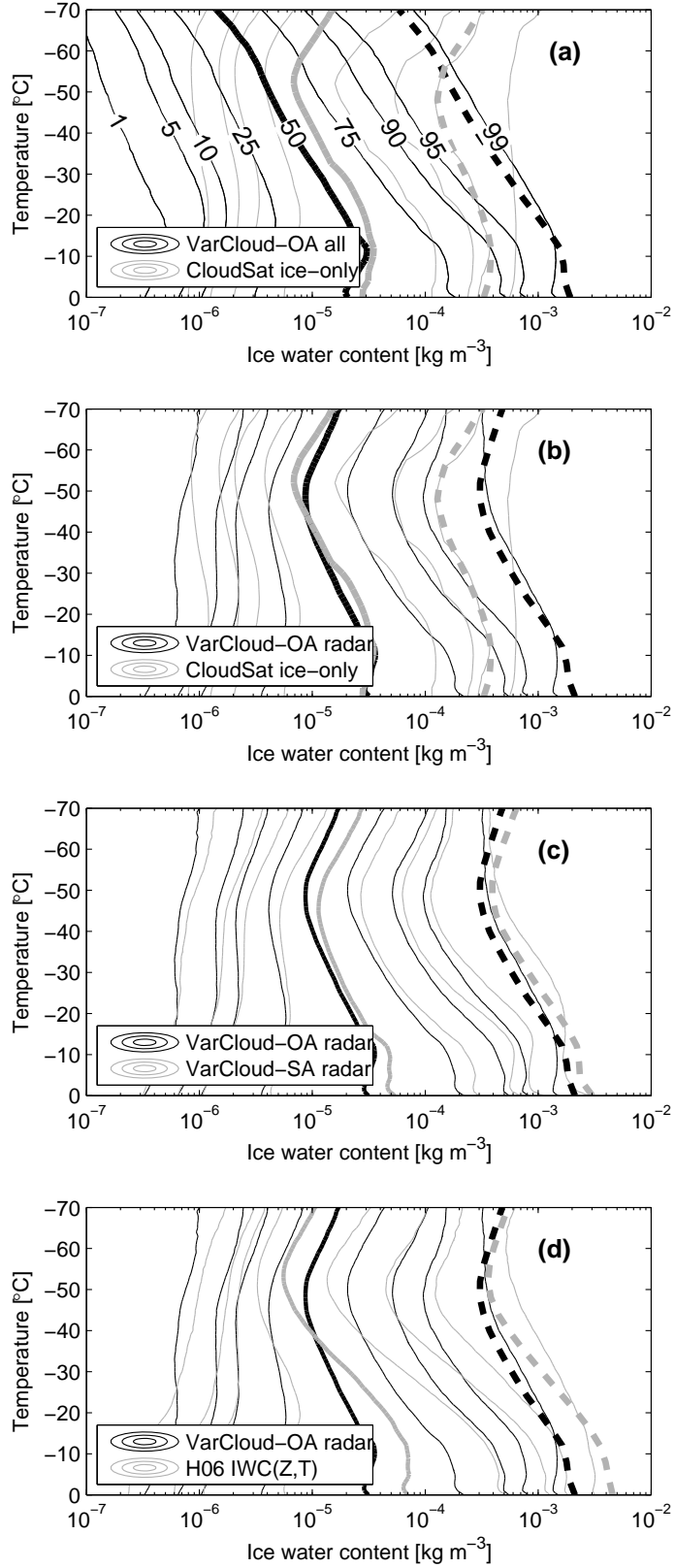


FIG. 5. In-cloud cumulative distribution of IWC versus  $T$ . From left to right, thin contours show the cumulative percentiles at 1%, 5%, 10%, 25%, 75%, 90%, 95%, 99%. Thick solid lines are the medians (50%) and dashed lines are the means as shown in Figure 4(a–e). (a) VarCloud-OA all (black) and CloudSat ice-only (grey); (b) VarCloud-OA radar (black) and CloudSat ice-only (grey); (c) VarCloud-OA radar (black) and VarCloud-SA radar (grey); (d) VarCloud-OA radar (black) and H06 (grey). Data are from July 2006. 18

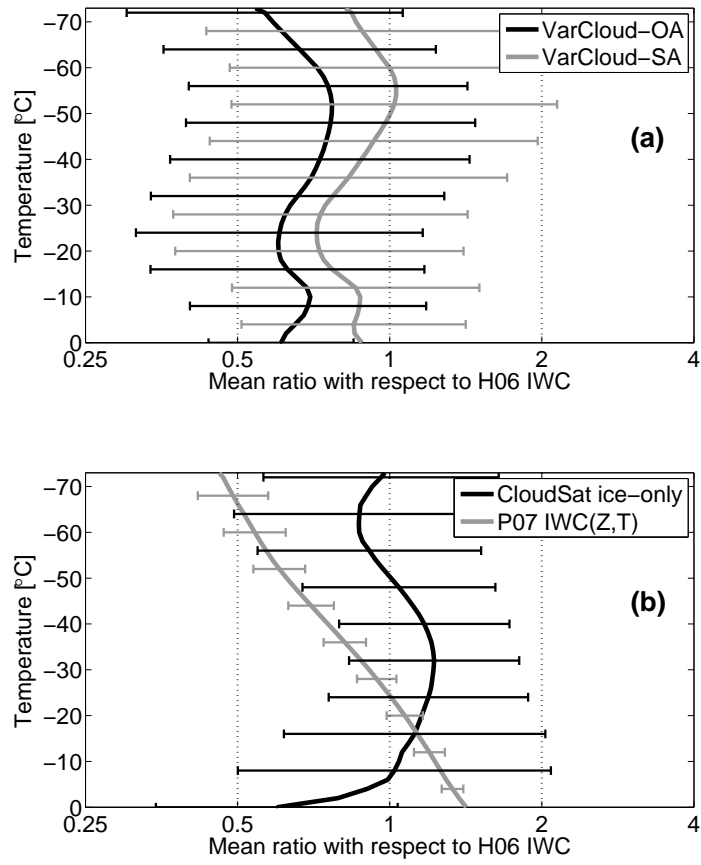


FIG. 6. Mean IWC ratio  $\mathcal{R}$  given by (13) versus temperature. (a) Mean ratios with control H06 (2) and product “R” VarCloud-OA (black) and VarCloud-SA (grey). (b) As (a), but with product “R” CloudSat ice-only (black) and P07 (grey). Rms differences are shown as error bars. Dotted lines show the -50%, 0%, and +100% difference from left to right. Data are from July 2006.

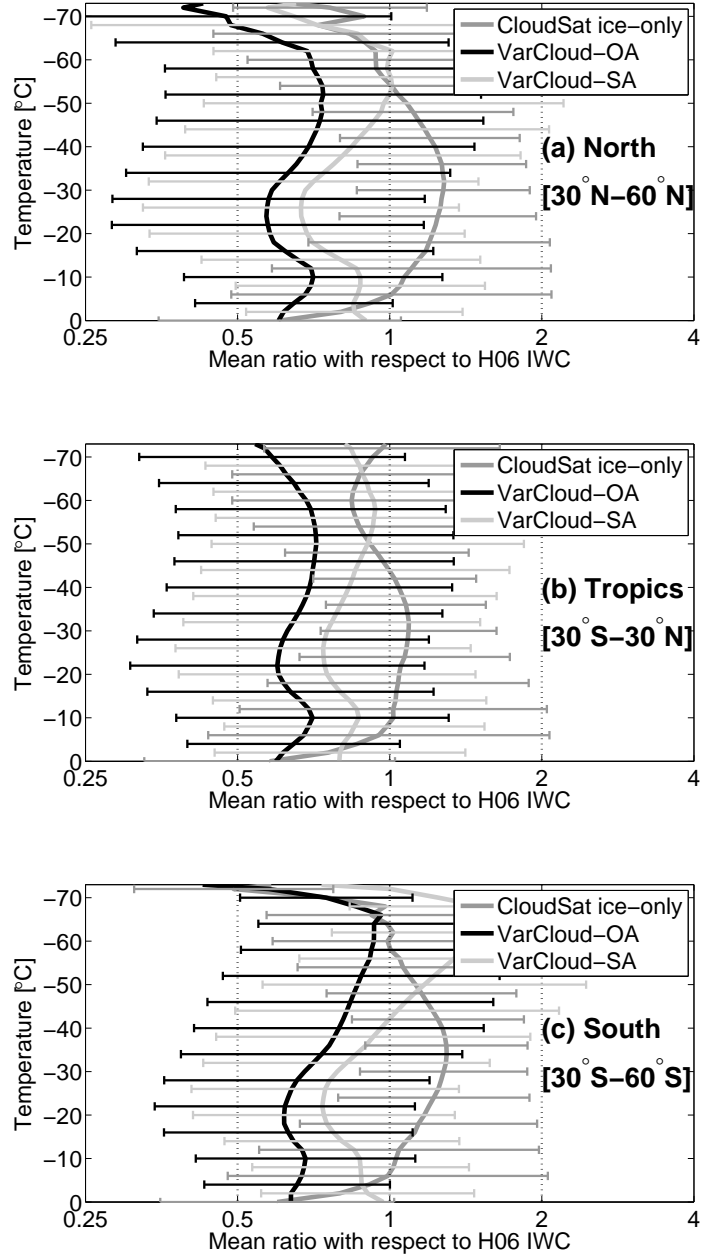


FIG. 7. Mean IWC ratio  $\mathcal{R}$  with control H06 as in Figure 6 split by different zonal regions (not showing P07). (a) Northern hemisphere 30°N–60°N; (b) tropics 30°S–30°N; (c) southern hemisphere 30°S–60°S. Rms differences are shown as error bars. Dotted lines show the  $-50\%$ ,  $0\%$ , and  $+100\%$  difference from left to right. Data are from July 2006.

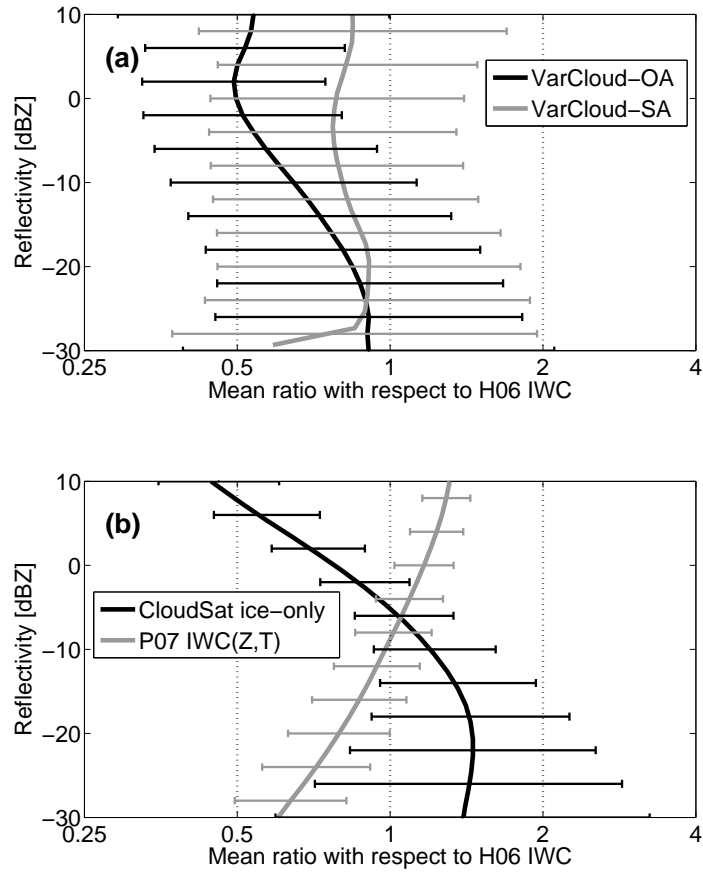


FIG. 8. (a) Mean IWC ratio  $\mathcal{R}$  versus radar reflectivity factor  $Z_e$  (dBZ). Shown are the ratios with control H06 for VarCloud-OA (black) and VarCloud-SA (grey). (b) As (a), but with CloudSat ice-only (black) and P07 (grey). Rms differences are shown as error bars. Dotted lines show the  $-50\%$ ,  $0\%$ , and  $+100\%$  difference from left to right. Data are from July 2006.

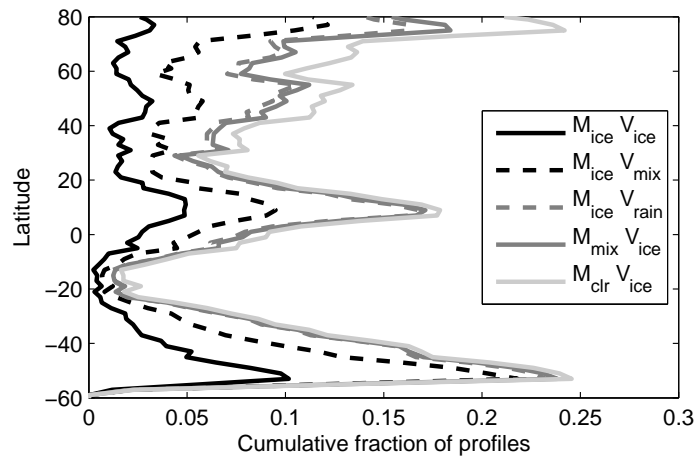


FIG. 9. Overview of joint MODIS (“M”) and VarCloud (“V”) observations of ice clouds for daytime overpasses in July 2006. Cumulative fraction of total number of profiles is shown per latitude, with combinations of cloud phase retrievals: (1) MODIS and VarCloud retrieve ice-only; (2) MODIS retrieves ice, but VarCloud also retrieves liquid (no rain); (3) MODIS retrieves ice, but VarCloud determines that there is rain in the profile; (4) VarCloud observes an ice-only profile, but MODIS retrieves a mixed, liquid, or undetermined cloud phase; (5) VarCloud observes an ice-only profile, but MODIS determines a clear profile.

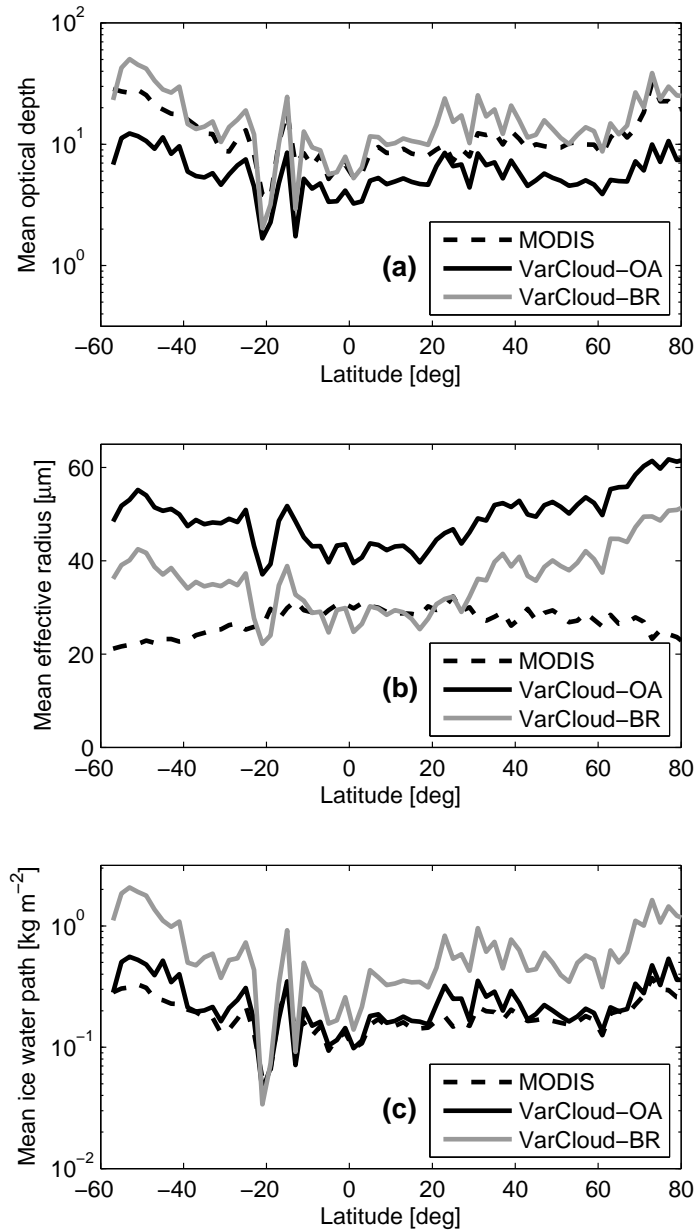


FIG. 10. An ice-cloud-only comparison between MODIS (dashed), VarCloud-OA (black), and VarCloud-BR (grey) retrievals of (a)  $\tau$ ; (b)  $\langle r_e \rangle$ ; and (c) IWP; showing the in-cloud zonal averages for July 2006. Only joint observations of ice-only profiles are included.

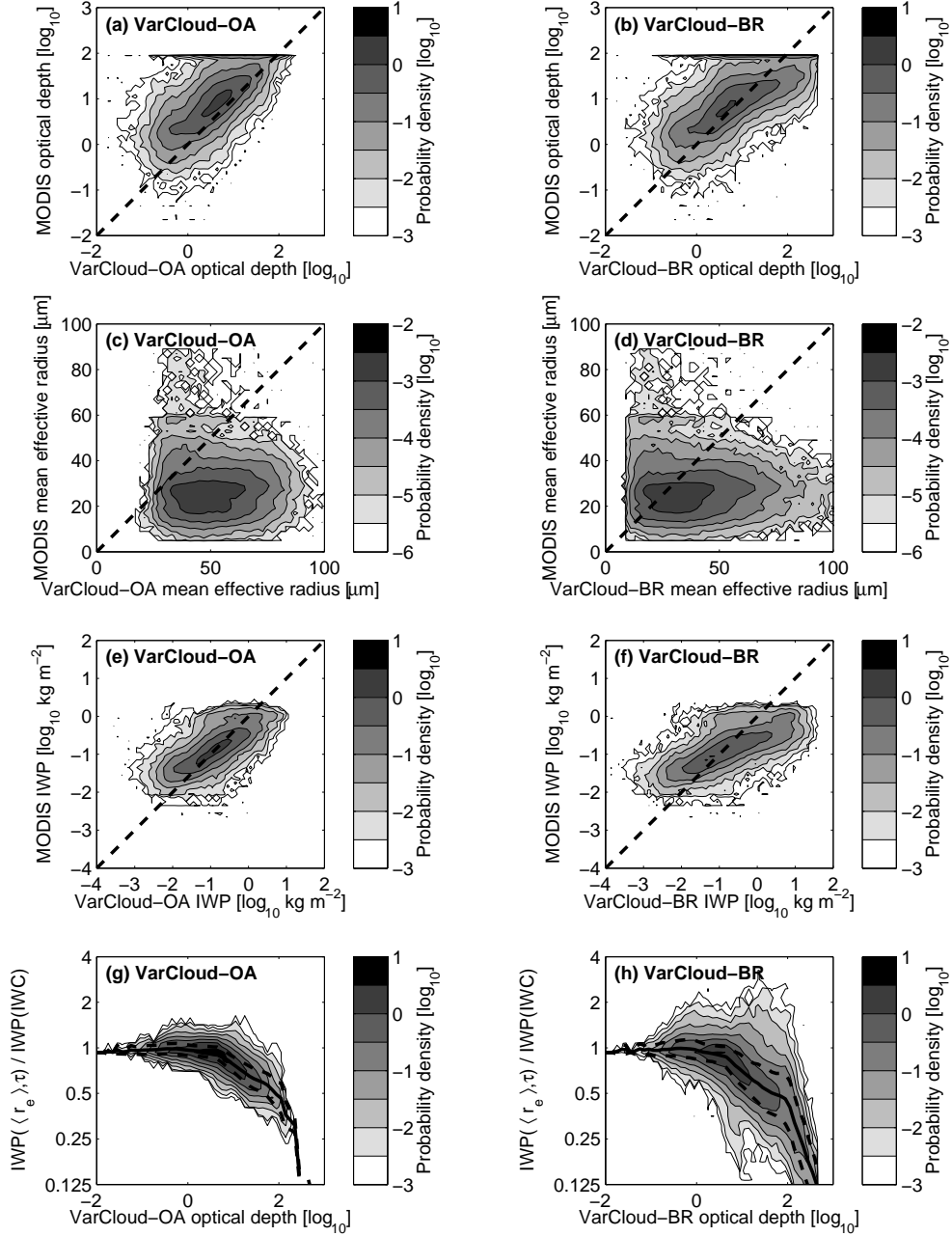


FIG. 11. (a–f) An ice-cloud-only comparison between MODIS and VarCloud for joint ice-cloud retrievals in terms of  $\tau$  with (a) VarCloud-OA and (b) VarCloud-BR; in terms of  $\langle r_e \rangle$  with (c) VarCloud-OA and (d) VarCloud-BR; in terms of IWP with (e) VarCloud-OA and (f) VarCloud-BR. (g–h) A comparison between IWP retrievals showing the ratio between IWP retrieved using (5) with  $\langle r_e \rangle$  for the top 5 cloud optical depths and  $\max(\tau) < 100$ , divided by IWP as the integral over IWC, versus VarCloud retrievals of  $\tau$ , for (g) VarCloud-OA and (h) VarCloud-BR. Data are from July 2006 and only joint observations of ice-only profiles are included. Dashed lines in (a–f) indicate the 1 : 1 ratio. Solid lines in (g–h) show the mean ratio and dashed lines show rms differences. Probability densities are per  $[\log_{10}]^2$  for  $\tau$ , per  $[\mu\text{m}]^2$  for  $\langle r_e \rangle$ , per  $[\log_{10} \text{ kg m}^{-2}]^2$  for IWP, and per  $[\log_{10} \log_2]$  for mean IWP ratio versus  $\tau$ .